Magnetization Density Distribution of Sr_2IrO_4: Deviation from a Local $j_{\mathrm{eff}} = 1/2$ Picture

Jaehong Jeong,[1,2,*] Benjamin Lenz,[3,4] Arsen Gukasov,[1] Xavier Fabrèges,[1] Andrew Sazonov,[5] Vladimir Hutanu,[5] Alex Louat,[6] Dalila Bounoua,[1] Cyril Martins,[7] Silke Biermann,[3,8,9,10] Véronique Brouet,[6] Yvan Sidis,[1] and Philippe Bourges[1,†]

[1]*Université Paris-Saclay, CNRS, CEA, Laboratoire Léon Brillouin, 91191 Gif-sur-Yvette, France*
[2]*Center for Correlated Electron Systems, Institute for Basic Science (IBS), Seoul National University, Seoul 08826, Korea*
[3]*Centre de Physique Théorique, Ecole Polytechnique, CNRS UMR7644, Institut Polytechnique de Paris, 91128 Palaiseau Cedex, France*
[4]*IMPMC, Sorbonne Université, CNRS, MNHN, IRD, 4 Place Jussieu, 75252 Paris, France*
[5]*Institute of Crystallography, RWTH Aachen University and Jülich Centre for Neutron Science (JCNS) at Heinz Maier-Leibnitz Zentrum (MLZ), 85747 Garching, Germany*
[6]*Laboratoire de Physique des Solides, Université Paris-Sud, UMR 8502, 91405 Orsay, France*
[7]*Laboratoire de Chimie et Physique Quantiques, UMR 5626, Université Paul Sabatier, 118 Route de Narbonne, 31400 Toulouse, France*
[8]*Collège de France, 11 Place Marcelin Berthelot, 75005 Paris, France*
[9]*Department of Physics, Division of Mathematical Physics, Lund University, Professorsgatan 1, 22363 Lund, Sweden*
[10]*European Theoretical Spectroscopy Facility, 91128 Palaiseau, France*

(Received 3 July 2019; revised 25 April 2020; accepted 29 July 2020; published 25 August 2020)

5*d* iridium oxides are of huge interest due to the potential for new quantum states driven by strong spin-orbit coupling. The strontium iridate Sr_2IrO_4 is particularly in the spotlight because of the so-called $j_{\mathrm{eff}} = 1/2$ state consisting of a quantum superposition of the three local t_{2g} orbitals with, in its simplest version, nearly equal populations, which stabilizes an unconventional Mott insulating state. Here, we report an anisotropic and aspherical magnetization density distribution measured by polarized neutron diffraction in a magnetic field up to 5 T at 4 K, which strongly deviates from a local $j_{\mathrm{eff}} = 1/2$ picture even when distortion-induced deviations from the equal weights of the orbital populations are taken into account. Once reconstructed by the maximum entropy method and multipole expansion model refinement, the magnetization density shows four cross-shaped positive lobes along the crystallographic tetragonal axes with a large spatial extent, showing that the *xy* orbital contribution is dominant. The analogy to the superconducting copper oxide systems might then be weaker than commonly thought.

DOI: 10.1103/PhysRevLett.125.097202

Sr_2IrO_4 possesses a tetragonal structure with $I4_1/acd$ space group in which the IrO_6 octahedra are rotated by $\approx 11°$ around the *c* axis with an opposite phase for the neighboring Ir ions, and displays antiferromagnetic order below $T_N \approx 230$ K [1–5]. Strong spin-orbit coupling stabilizes an unconventional Mott insulating ground state, which is commonly described by a spin-orbital product state within a so-called $j_{\mathrm{eff}} = 1/2$ model [2,6–8]. In the simplest version of this model, 5*d* electrons at the Ir^{4+} ($5d^5$) ions occupy the t_{2g} states with an effective angular momentum $l_{\mathrm{eff}} = 1$, which are split by the relatively large spin-orbit coupling into a $j_{\mathrm{eff}} = 1/2$ doublet and a $j_{\mathrm{eff}} = 3/2$ quartet. The Coulomb repulsion induces a gap in the narrow half-filled $j_{\mathrm{eff}} = 1/2$ band and stabilizes the Mott insulating state with the pseudospin $j_{\mathrm{eff}} = 1/2$ [2,7], which consists of three equally populated spin-orbital components in the t_{2g} band [Fig. 1(a)]:

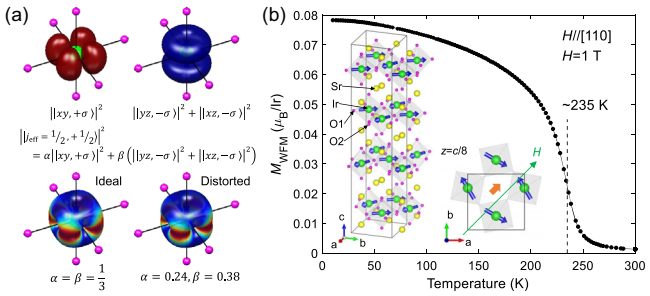

FIG. 1. The $j_{\mathrm{eff}} = 1/2$ states and uniform magnetization of Sr_2IrO_4. (a) Illustration of the electron and spin density distributions for the ideal (distorted) $j_{\mathrm{eff}} = 1/2$, $m_j = 1/2$ state, which consists of three (nearly) equally populated t_{2g} orbitals with mixed spin states. The red and blue colors represent spin-up and spin-down states, respectively.(b) The magnetization vs temperature curve under $H = 1$ T ($H//[110]$). Sr_2IrO_4 exhibits a weak ferromagnetic moment inherited from the AF-II order transition [3] at ≈235 K. The inset shows the crystal and magnetic structure of Sr_2IrO_4 for an applied magnetic field along $H//[110]$.

$$\left|j_{\mathrm{eff}}=\frac{1}{2},\pm\frac{1}{2}\right\rangle=\frac{1}{\sqrt{3}}(|xy,\pm\sigma\rangle\pm|yz,\mp\sigma\rangle+i|xz,\mp\sigma\rangle), \tag{1}$$

where $\pm\sigma$ denotes the spin of the electrons.

While resonant and inelastic x-ray scattering [6,9] gave credit to a description in terms of these $j_{\mathrm{eff}}=1/2$ states [10], the simple description with equal weights for the orbital populations has been questioned owing to a tetragonal distortion that is not negligible [11–13]. Indeed, the simplest model with equal weights is realized only for a perfect cubic symmetry, while any lattice distortions (compression, elongation, or tilting of the octahedra around the c axis) split the t_{2g} orbitals into three nondegenerate Kramers doublets [7,11,13–16], driving the lowest energy state away from the equal weight case of Eq. (1). In the following, we adopt the nomenclature common to the field and still refer to the states that diagonalize the local Hamiltonian in the presence of the distortions present in Sr_2IrO_4 as $j_{\mathrm{eff}}=1/2$ and $j_{\mathrm{eff}}=3/2$ states. Figure 1(a) compares the electron and spin density distributions corresponding to the perfectly cubic and the distorted cases.

In addition, a strong hybridization between Ir $5d$ and O $2p$ orbitals, which seems to be natural for a large spatial extent of $5d$ orbitals, has been proposed to account for a large reduction of the ordered magnetic moment [2], as well as for antiferromagnetic (AFM) exchange interactions between the nearest-neighboring Ir ions and for the canted magnetic moments following the octahedral rotations [7,15]. The strong hybridization of the d orbitals with the p orbitals of the ligand oxygen is reminiscent of K_2IrCl_6 [17] and the isostructural ruthenate $Ca_{1.5}Sr_{0.5}RuO_4$ [18], where similar covalency effects have been reported. In Sr_2IrO_4, recent muon spin relaxation measurements have suggested the formation of oxygen moments [19] and charge redistribution between adjacent IrO_2 and SrO layers has been revealed using electron spin resonance measurement [20]. Further, unusual magnetic multipoles have been proposed to be observed by neutron diffraction [21], and recently a hidden magnetic order having the same symmetry as a loop-current state has been observed by polarized neutron diffraction [22].

The magnetic moments of Ir ions are confined in the ab plane and track the staggered octahedral rotation in an $-+$ $+-$ sequence along the c axis in the unit cell [3]. Owing to this canted AFM structure, each IrO_2 layer has a weak ferromagnetic (WFM) moment along the principal crystallographic axis in the ab plane at zero magnetic field. This WFM moment is compensated due to the $-++-$ stacking sequence, whereas, in a magnetic field higher than $H_c\approx 0.3$ T applied in the ab plane [2,3], a net homogeneous WFM moment appears in the plane [inset of Fig. 1(b)] above the metamagnetic transition. Remarkably, this WFM moment follows the direction of applied magnetic field in the ab plane [23–25] and attains a saturation value of $\approx 0.08\ \mu_B$/Ir in the field of 1 T [23]. In the current experiment, a uniform magnetic field (H) up to 5 T has been applied along the vertical direction [Fig. 2(a)]. The IrO_6 octahedral rotation generates two additional magnetic terms in the simple Heisenberg-type Hamiltonian [25]: J_z and Dzyaloshinskii-Moriya terms, which restrict the angle between adjacent pseudospins to $\pi+2\alpha$ with the octahedral rotation angle α [7]. However, these interactions do not break the in-plane rotational symmetry as the pseudospins are free to rotate in the plane while keeping the same canting angle between them [the situation is shown in the inset of Fig. 1(b) for a field applied along the [110] direction]. Therefore, under the applied magnetic field, the WFM moment does not interlock with the rotation of IrO_6 octahedra in contrast to the AFM staggered moment at zero field.

The existence of this WFM allows us to probe the magnetization density distribution in crystals by polarized neutron diffraction (PND). This technique is unique because it provides direct information about the three-dimensional distribution of the magnetization throughout the unit cell, which in turn allows for a determination of the symmetry of occupied orbitals. This method has been successfully used in the study of ferromagnetic ruthenate $Ca_{1.5}Sr_{0.5}RuO_4$, isostructural to Sr_2IrO_4, where an anomalously high spin density at the oxygen site and the xy character of the Ru d orbitals have been reported [18].

The typical experimental setup for PND, shown in Fig. 2(a), consists of a neutron polarizer, a flipping device that reverses the incident neutron polarization, a magnet, and a detector. The sample is magnetized by a magnetic field applied along the vertical axis and scattering intensities of Bragg reflections for the two opposite states (spin-up and spin-down) of the incident polarization are measured. They are used to calculate the so-called flipping ratio, allowing access to the Fourier components of the magnetization density as

$$R_{\mathrm{PND}}=\frac{I_\uparrow}{I_\downarrow}=\frac{F_N^2+2p\sin^2\alpha F_N F_M+\sin^2\alpha {F_M}^2}{F_N^2-2pe\sin^2\alpha F_N F_M+\sin^2\alpha {F_M}^2}, \tag{2}$$

where F_N is the nuclear structure factor and F_M is the magnetic structure factor. p and e are the polarization efficiency of the polarizer and flipper, respectively, and α is the angle between the scattering vector and the magnetization [26]. The flipping ratios R_{PND} of more than 280 (hkl) reflections were measured in the WFM state above the metamagnetic transition at 2 K for two magnetic field orientations, $H\|[010]$ and $H\|[\bar{1}10]$ (well above the critical field $H_c\approx 0.3$ T [6,25]). The measured intensities for two orientations were averaged [26]. As shown in Fig. 2(b), the magnetic structure factors F_M were directly obtained from the measured flipping ratios by using Eq. (2) and known nuclear structure factors F_N. For convenience, the amplitudes are given in Bohr magnetons, normalized by the number of Ir atoms (8) in the unit cell and taken in absolute

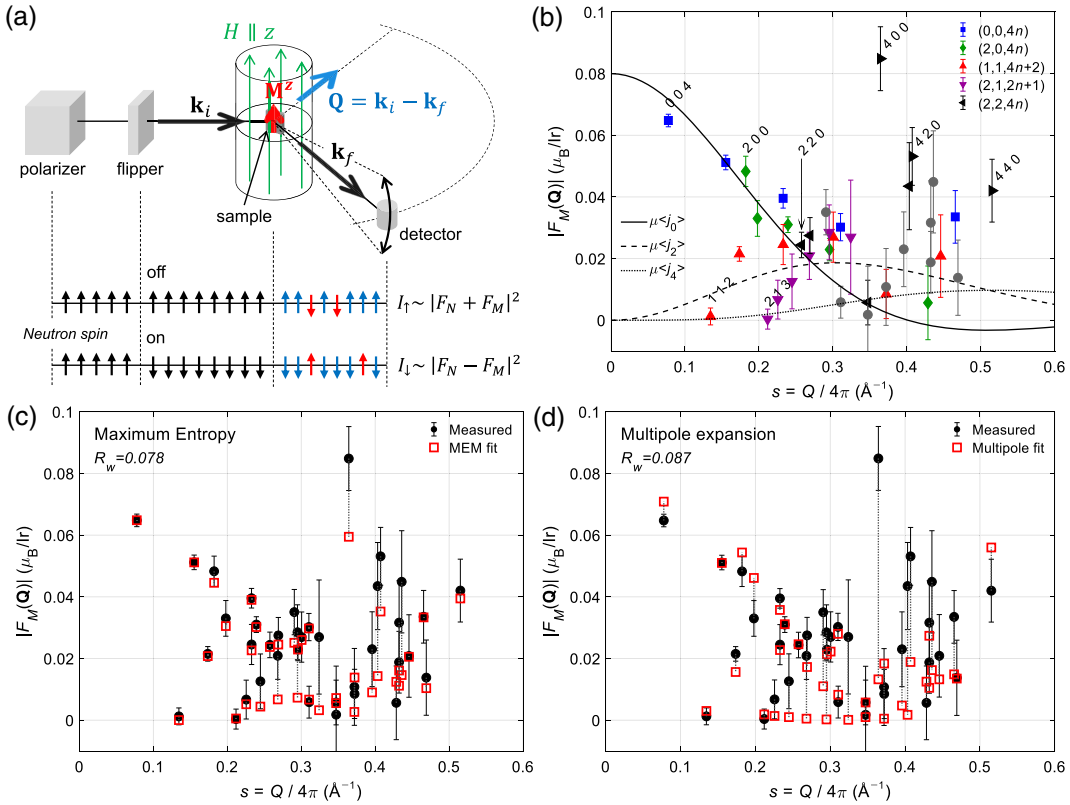

FIG. 2. Polarized neutron diffraction setup and measured neutron magnetic structure factor of Sr_2IrO_4. (a) The experimental setup for a polarized neutron diffraction experiment. The arrows at the bottom denote a spin polarization of neutrons. The vertical direction corresponds to either the [010] or $[\bar{1}10]$ crystallographic direction for each sample orientation [26]. (b) The magnetic structure factor of all measured momentum transfer Q with the theoretical radial integrals $\langle j_n \rangle$ for isolated Ir^{4+} ions. A series of reflections along the $(0, 0, l)$ are highlighted: $(0, 0, 4n)$ in blue squares, $(2, 0, 4n)$ in green diamonds, $(1, 1, 4n + 2)$ in red up-triangles, $(2, 1, 2n + 1)$ in purple down-triangles, and $(2, 2, 4n)$ in black left-triangles. The (4,0,0), (4,2,0), and (4,4,0) are also presented in black right-triangles, and the rest in grey circles. Measured and fitted magnetic structure factors $|F_M(\mathbf{Q})|$ for (c) the optimized MEM result and (d) optimized multipole expansion result.

values to remove alternating signs of the phase factor. The amplitude, $F_M(0)$, is imposed in agreement with the saturation moment ($0.08\mu_B$/Ir) given by the uniform magnetization measurement [23].

In the *dipole approximation*, i.e., at low momentum transfer, $F_M(Q)$ is usually described by a smooth decreasing function of Q, called the magnetic form factor, corresponding to a linear combination of radial integrals calculated from the electronic radial wave function. Instead, in Fig. 2(b) one observes a large distribution of the measured structure factor indicating unusually large anisotropy. That large anisotropy is explained by a predominance of the xy orbital as shown below using the reconstruction of the magnetization density in real space. The theoretical radial integrals $\langle j_n \rangle$ for an isolated Ir^{4+} ion [34] are also shown in Fig. 2(b) for comparison. We recall that $\langle j_2 \rangle$, $\langle j_4 \rangle$ and higher-order integrals are needed to describe the departures from spherical symmetry. As seen from Fig. 2, except for the $(0, 0, l)$ reflections decreasing gradually with increasing Q, the majority of reflections strongly deviate from any expected smooth curve. Moreover, while the $(0, 0, 4n)$, $(2, 0, 4n)$, and $(2, 2, 4n)$ reflections are close to the $\langle j_0 \rangle$ curve in a small Q region, the $(1, 1, 4n + 2)$ and $(2, 1, 2n + 1)$ reflections deviate from it quite strongly. This indicates an aspherical magnetization density, which is typical of ions with one or two unpaired electrons in the d orbitals [17,35,36]. In addition, one can see that high-Q reflections like the (4,0,0), (4,2,0), and (4,4,0) ones show anomalously large values.

Next, a real space visualization has been performed by a reconstruction of the magnetization density using two different very well-established and widely used approaches: a model-free maximum entropy method (MEM) [37] and a quantitative refinement using the multipole expansion of the density function [38]. Both techniques have advantages and limits and should be employed where they are the most efficient. Typically, no assumption is made for the initial magnetization distribution in MEM, whereas the d orbitals' shape is constrained in the multipole expansion.

Since the crystal structure is centrosymmetric, the magnetization density can be directly reconstructed from the measured magnetic structure factors by MEM [37].

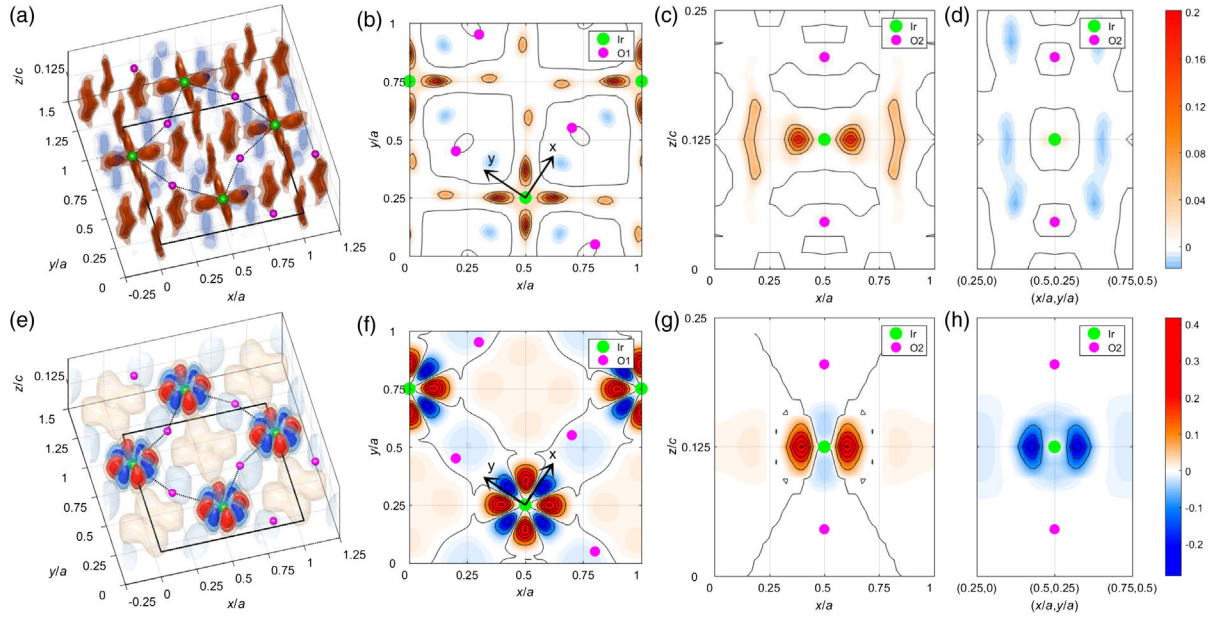

FIG. 3. Magnetization density distribution reconstructed by MEM and multipole expansion refinement. 3D magnetization density distribution on the $z = c/8$ layer reconstructed by (a) the MEM and (e) the multipole expansion model refinement. Isosurfaces encompassing 30%, 50%, and 70% of the volume density are plotted with a descending opacity according to their isovalues. Red and blue surfaces denote positive and negative magnetizations, respectively. The solid square and dotted lines denote the unit cell and Ir-O bonds, respectively. Sliced density contour maps at (b),(f) $(x, y, c/8)$, (c),(g) $(x, a/4, z)$, and (d),(h) $(a/4 + x, x, z)$ are also shown for both methods. The contour step is 0.04 and $0.08\mu_B/$ Å^3 for (b)–(d) and (f)–(h), respectively. The black arrows correspond to the Ir-O bonding directions.

Figure 3(a)–3(d) shows the three-dimensional magnetization density reconstructed by using a conventional flat density prior. A positive magnetization density in red denotes a magnetic moment density parallel to the applied magnetic field and a negative one in blue is antiparallel. There are three key features to be noted in the figure. First, the magnetization density at Ir sites has four positive density lobes directed along the a, b axes corresponding to a dominant positive magnetization density of d_{xy} orbital symmetry [Fig. 3(b)]. The two other components of the effective $j_{\text{eff}} = 1/2$ state model, d_{yz} and d_{xz}, which would form an axially symmetric doughnut-shaped density above and below the xy plane [see Fig. 1(a)], do not appear as seen in Fig. 3(c) and 3(d). Thus, the WFM density originates predominantly from the xy orbital [a schematic illustration of the magnetic components in this situation is given in the Supplemental Material (Fig. S4) [26], in contrast with the local $j_{\text{eff}} = 1/2$ picture]. Second, positive density lobes are very strongly elongated in such a way that some magnetization density is delocalized well beyond of the IrO_6 octahedra. Third, contrary to the expectation of strong iridium oxygen ligand hybridization, no visible induced magnetization density appears at the oxygen sites. Actually, no noticeable magnetization (within the error bars) has been found at the oxygen sites in any of dozens of measured $(2, 1, 2n + 1)$ reflections where oxygen atoms contribute the most. This is in contrast to the isostructural $4d$ compound $Ca_{1.5}Sr_{0.5}RuO_4$, where ~20% of the magnetic moment is transferred to the in-plane O sites [18]. However, one can notice the presence of a negative magnetic density, mostly along the Ir-O direction, existing between the large positive lobes. In fact, a significant negative magnetization density as large as half of the net moment is essential for a better description in the MEM analysis [26].

To confirm the symmetry found by MEM, multipole expansion was performed for an alternative refinement of the WFM density [38,39]. It is composed of radial and angular parts: Slater-type radial wave functions and real spherical harmonic density functions [26]. In Fig. 3(e)–3(h), the magnetization density distribution with the best refinement is shown. The main positive magnetization density lobes located between the local x and y axis appear clearly, which corresponds to the d_{xy} symmetry. Therefore, the multipole expansion model fully confirms the d_{xy} symmetry found by MEM. A benefit of the multipole method is to determine the contribution of all five d orbitals to the magnetization. Using the orbital-multipole relations [38], the magnetic moments on each orbital were obtained as +0.48, −0.051, −0.035, and −0.314 μ_B/Ir for d_{xy}, $d_{yz/xz}$, d_{z^2}, and $d_{x^2-y^2}$, respectively. Thus, a positive d_{xy} and to a lesser extent a negative $d_{x^2-y^2}$ orbital are dominant in the refinement (the latter effect is minor in the MEM method), while the $d_{yz/xz}$ orbitals are barely populated. Interestingly,

the admixture of $d_{x^2-y^2}$ character to the $j_{\mathrm{eff}} = 1/2$ orbital also has been found in first principles simulations [40].

It is obvious that the refinement of multipoles with a single radial exponent cannot fit the widely delocalized density. Therefore, we introduce in the refinement a second radial exponent to describe the delocalized Ir density. Such a model shows a considerably better agreement factor ($R_w \sim 0.09$) compared to the model with a single radial exponent ($R_w \sim 0.18$) (see Supplemental Material [26], Sec. V). That result confirms the anomalously large spatial extent of the magnetization density of Ir found by the MEM analysis. To appreciate the relevance of the obtained magnetization maps, we calculate the magnetic structure factors from the optimized MEM and multipoles results. By plotting them along with the measured ones in Fig. 2(c) (for MEM) and Fig. 2(d) (for multipoles), one sees that the calculated densities with MEM better reproduce the experimental data.

While the standard modeling of layered iridates by means of an anisotropic super-exchange Hamiltonian within the *effective local* $j_{\mathrm{eff}} = 1/2$ picture correctly captures the WFM moment of the ground state and explains the most salient magnetic properties of Sr_2IrO_4 [7,10,15,16,41], this local $j_{\mathrm{eff}} = 1/2$ model is at odds with the present findings: its simplified version with equal orbital weights would suggest a homogeneous magnetization density, while taking into account distortions would, even worse, enhance the xz and yz orbital weight of the hole and thus of the WFM [see Fig. 1(a)].

These considerations give an additional twist to the exotic properties of Sr_2IrO_4 and the possibilities of modeling them, as well as to the relationship to superconducting copper oxides. Recently, our PND results have been interpreted in terms of spin anapole [42], pointing toward the existence of multipole correlations that goes beyond the local $j_{\mathrm{eff}} = 1/2$ picture. An alternative interpretation based on a momentum-dependent composition of the orbital carrying the hole in terms of atomic t_{2g} states will be published elsewhere [43]. In this type of model, the hole resides in an orbital that results from a nonlocal, that is, a $\mathbf{k}$-dependent superposition of Wannier functions of t_{2g} character. In this light, it is less surprising that neither the simplified $j_{\mathrm{eff}} = 1/2$ picture discussed above nor the state that takes into account the structural distortions but remains restricted to a local superposition of atomic orbitals describes our present experimental findings.

In summary, using PND we have evidenced a magnetization density distribution in Sr_2IrO_4 that is inconsistent with the local $j_{\mathrm{eff}} = 1/2$ picture. The measured magnetic structure factor shows a strong axial anisotropy and anomalous values at large Q, which indicate an aspherical magnetization density distribution with a significant orbital contribution. Real space visualization exhibits a dominant d_{xy} orbital character with highly elongated lobes of Ir magnetization densities toward the next Ir atoms. Although a strong $d-p$ hybridization is expected in Sr_2IrO_4, the magnetization density at the ligand oxygen sites is barely present. Our results elucidate that the ground state of Sr_2IrO_4 substantially deviates from the commonly accepted local $j_{\mathrm{eff}} = 1/2$ state.

We acknowledge support from the projects NirvAna (Contract No. ANR-14-OHRI-0010) and SOCRATE (ANR-15-CE30-0009-01) of the French Agence Nationale de la Recherche (ANR), by the Investissement dAvenir LabEx PALM (Grant No. ANR-10-LABX-0039-PALM), and by the European Research Council under Grant Agreement CorrelMat-617196 for financial support. J. J. was supported by an Incoming CEA fellowship from the CEA-Enhanced Eurotalents program, co-funded by the FP7 Marie-Sklodowska-Curie COFUND program (Grant Agreement No. 600382) and by the Institute of Basic Science (IBS) in Korea (Grant No. IBS-R009-G1). Instrument POLI at Maier-Leibnitz Zentrum (MLZ) Garching is operated in cooperation with RWTH Aachen University and Forschungszentrum Jülich GmbH (Jülich-Aachen Research Alliance JARA). We thank Professor S. V. Lovesey for valuable comments on the manuscript and J. Porras for scientific discussions.

*Corresponding author.
hoho4@snu.ac.kr
†Corresponding author.
philippe.bourges@cea.fr

[1] Q. Huang, J. Soubeyroux, O. Chmaissem, I. N. Sora, A. Santoro, R. J. Cava, J. J. Krajewski, and W. F. Peck, J. Solid State Chem. **112**, 355 (1994).
[2] B. J. Kim, H. Jin, S. J. Moon, J.-Y. Kim, B.-G. Park, C. S. Leem, J. Yu, T. W. Noh, C. Kim, S.-J. Oh, J.-H. Park, V. Durairaj, G. Cao, and E. Rotenberg, Phys. Rev. Lett. **101**, 076402 (2008).
[3] F. Ye, S. Chi, B. C. Chakoumakos, J. A. Fernandez-Baca, T. Qi, and G. Cao, Phys. Rev. B **87**, 140406(R) (2013).
[4] C. Dhital, T. Hogan, Z. Yamani, C. de la Cruz, X. Chen, S. Khadka, Z. Ren, and S. D. Wilson, Phys. Rev. B **87**, 144405 (2013).
[5] N. H. Sung, H. Gretarsson, D. Proepper, J. Porras, M. Le Tacon, A. V. Boris, B. Keimer, and B. J. Kim, Philos. Mag. **96**, 413 (2016).
[6] B. J. Kim, H. Ohsumi, T. Komesu, S. Sakai, T. Morita, H. Takagi, and T. Arima, Science **323**, 1329 (2009).
[7] G. Jackeli and G. Khaliullin, Phys. Rev. Lett. **102**, 017205 (2009).
[8] F. Wang and T. Senthil, Phys. Rev. Lett. **106**, 136402 (2011).
[9] J. Kim, D. Casa, M. H. Upton, T. Gog, Y.-J. Kim, J. F. Mitchell, M. van Veenendaal, M. Daghofer, J. van den Brink, G. Khaliullin, and B. J. Kim, Phys. Rev. Lett. **108**, 177003 (2012).
[10] J. Bertinshaw, J. Y. Kim, G. Khaliullin, and B. J. Kim, Annu. Rev. Condens. Matter Phys. **10**, 315 (2019).

[11] L. C. Chapon and S. W. Lovesey, J. Phys. Condens. Matter **23**, 252201 (2011).
[12] D. Haskel, G. Fabbris, M. Zhernenkov, P. P. Kong, C. Q. Jin, G. Cao, and M. van Veenendaal, Phys. Rev. Lett. **109**, 027204 (2012).
[13] M. Moretti Sala, S. Boseggia, D. F. McMorrow, and G. Monaco, Phys. Rev. Lett. **112**, 026403 (2014).
[14] A. Abragam and B. Bleaney, *Electron Paramagnetic Resonance of Transition Ions* (Oxford University Press, Oxford, 2012).
[15] N. B. Perkins, Y. Sizyuk, and P. Wölfle, Phys. Rev. B **89**, 035143 (2014).
[16] B. Lenz, C. Martins, and S. Biermann, J. Phys. Condens. Matter **31**, 293001 (2019).
[17] J. W. Lynn, G. Shirane, and M. Blume, Phys. Rev. Lett. **37**, 154 (1976).
[18] A. Gukasov, M. Braden, R. J. Papoular, S. Nakatsuji, and Y. Maeno, Phys. Rev. Lett. **89**, 087202 (2002).
[19] M. Miyazaki, R. Kadono, M. Hiraishi, A. Koda, K. M. Kojima, K. Ohashi, T. Takayama, and H. Takagi, Phys. Rev. B **91**, 155113 (2015).
[20] N. A. Bogdanov, V. M. Katukuri, J. Romhányi, V. Yushankhai, V. Kataev, B. Büchner, J. van den Brink, and L. Hozoi, Nat. Commun. **6**, 7306 (2015).
[21] S. W. Lovesey and D. D. Khalyavin, J. Phys. Condens. Matter **26**, 322201 (2014).
[22] J. Jeong, Y. Sidis, A. Louat, V. Brouet, and P. Bourges, Nat. Commun. **8**, 15119 (2017).
[23] L. Fruchter, D. Colson, and V. Brouet, J. Phys. Condens. Matter **28**, 126003 (2016).
[24] M. Nauman, Y. Hong, T. Hussain, M. S. Seo, S. Y. Park, N. Lee, Y. J. Choi, W. Kang, and Y. Jo, Phys. Rev. B **96**, 155102 (2017).
[25] J. Porras, J. Bertinshaw, H. Liu, G. Khaliullin, N. H. Sung, J.-W. Kim, S. Francoual, P. Steffens, G. Deng, M. Moretti Sala, A. Efimenko, A. Said, D. Casa, X. Huang, T. Gog, J. Kim, B. Keimer, and B. J. Kim, Phys. Rev. B **99**, 085125 (2019).
[26] See Supplemental Material, which includes Refs. [27–33], at http://link.aps.org/supplemental/10.1103/PhysRevLett.125.097202 for the sample preparation and characterization (Sec. I), for details of PND measurements (Sec. II), for the data treatment methods (Sec. III), for details of the MEM analysis (Sec. IV), and for details of the multipole expansion analysis (Sec. V).
[27] A. Gukasov, A. Goujon, J.-L. Meuriot, C. Person, G. Exil, and G. Koskas, Physica (Amsterdam) **397B**, 131 (2007).
[28] A. Gukasov, S. Rodrigues, J.-L. Meuriot, T. Robillard, A. Sazonov, B. Gillon, A. Laverdunt, F. Prunes, and F. Coneggo, Phys. Procedia **42**, 150 (2013).
[29] J. Akimitsu, H. Ichikawa, N. Eguchi, T. Miyano, M. Nishi, and K. Kakurai, J. Phys. Soc. Jpn. **70**, 3475 (2001).
[30] C. Martins, Ph.D. thesis, Ecole Polytechnique, Palaiseau, 2010.
[31] S. Agrestini, C.-Y. Kuo, M. Moretti Sala, Z. Hu, D. Kasinathan, K.-T. Ko, P. Glatzel, M. Rossi, J.-D. Cafun, K. O. Kvashnina, A. Matsumoto, T. Takayama, H. Takagi, L. H. Tjeng, and M. W. Haverkort, Phys. Rev. B **95**, 205123 (2017).
[32] A. Paturle and P. Coppens, Acta Crystallogr. Sect. A **44**, 6 (1988).
[33] P. J. Brown and J. C. Matthewman, Rutherford Appleton Laboratory, Report No. RAL-93-009, 1993.
[34] K. Kobayashi, T. Nagao, and M. Ito, Acta Crystallogr. Sect. A **67**, 473 (2011).
[35] S. Shamoto, M. Sato, J. M. Tranquada, B. J. Sternlieb, and G. Shirane, Phys. Rev. B **48**, 13817 (1993).
[36] I. A. Zaliznyak and S.-H. Lee, Magnetic neutron scattering, Brookhaven Natioal Laboratory, USA, Technical Report, 2004.
[37] R. J. Papoular and B. Gillon, Europhys. Lett. **13**, 429 (1990).
[38] P. Coppens, *X-Ray Charge Densities and Chemical Bonding* (Oxford University Press, New-York, 1997), Vol. 4.
[39] N. K. Hansen and P. Coppens, Acta Crystallogr. Sect. A **34**, 909 (1978).
[40] C. Martins, M. Aichhorn, and S. Biermann, J. Phys. Condens. Matter **29**, 263001 (2017).
[41] C. Martins, B. Lenz, L. Perfetti, V. Brouet, F. Bertran, and S. Biermann, Phys. Rev. Mater. **2**, 032001 (2018).
[42] D. D. Khalyavin and S. W. Lovesey, Phys. Rev. B **100**, 224415 (2019).
[43] B. Lenz *et al.* (to be published).